Journal of Applied Fluid Mechanics, Vol. 16, No. 1, pp. 101-119, 2023.
Available online at www.jafmonline.net, ISSN 1735-3572, EISSN 1735-3645.
https://doi.org/10.47176/jafm.16.01.1226

Proper Orthogonal Decomposition Analysis of an Airfoil Performances under a Small Vortical Gust

M. M. Oueslati[1†], A. W. Dahmouni[1] and M. Ben Salah[2]

[1] *Laboratory of Wind Energy Management and Waste Energy Recovery, Research and Technologies Center of Energy, Ecoparck of Borj-Cedria, BP 95 Hammam lif, 2050, Tunisia*
[2] *Laboratory of Thermal Process, Research and Technologies Center of Energy, Ecoparck of Borj-Cedria, BP 95 Hammam lif, 2050, Tunisia*

†*Corresponding Author Email: mehdi.oueslati@crten.rnrt.tn*

(Received April 6, 2022; accepted August 24, 2022)

ABSTRACT

This paper investigates the performance of a non-symmetric airfoil in a perturbed flow for a low Reynolds number by creating small vortical structures. A newly designed two-dimensional numerical tool is used to examine the interaction between the NACA 23015 airfoil and the vortex shedding from a square cylinder. Different airfoil position ratios are numerically simulated concerning the square cylinder G/D (D: square cylinder diameter), the channel centerline T/d (d=D/2), and the vortices scale size D/c (c: airfoil chord length). Results show that the maximum values of the lift and drag aerodynamic coefficients are influenced by the airfoil's lateral and longitudinal positions. The Proper Orthogonal Decomposition (POD) method is used to identify the most energetic flow structures. For all simulated scenarios, it was found that the first two modes reflect the dominating coherent structures in the flow field. The results also show that a leading-edge vortex is formed over the airfoil. The observed phenomena of symmetric and antisymmetric shedding vortex mechanisms essentially depend on the lateral distance of the airfoil T/d and the vortex scale size D/c. However, the spectral analysis demonstrates that the shedding frequency mainly depends on the gap distance G/D.

Keywords: Airfoil aerodynamics; Numerical simulation; Vortex-airfoil interaction; Proper orthogonal decomposition; Coherent structures.

NOMENCLATURE

a_n	coefficients modes
(a,b,c)	interpolation coefficients
c	airfoil chord length
CL	Lift Coefficient
CD	Drag Coefficient
D	square characteristic length
$f_n(x)$	instantaneous velocity field of snapshots
G	gap distance
h	channel height
K	snapshot number
L	channel length
P	pressure
POD	Proper Orthogonal Decomposition
Re	Reynolds number
St	Strouhal number
T	longitudinal length
t	time
$\vec{U}$	velocity vector
u	axial velocity
u_0	velocity inlet
u_{avr}	average velocity
V_c	control volume
v	longitudinal velocity
(x,y)	space coordinates
ζ_n	POD eigenvectors
λ_n	POD eigenvalues
$\Phi_n(x)$	orthonormal POD eigenmodes
ψ	stream-function
ω	vorticity
$\langle ... \rangle$	ensemble averaging

1. INTRODUCTION

During the last few decades, there was a dramatic shift in the airfoils employment in low-Reynolds-number applications. Micro-Aerial Vehicles (MAV), small wind turbines, high-altitude Remotely Piloted Vehicles (RPV), and a variety of other industrial uses piqued their interest (Mueller and DeLaurier 2003; Mueller *et al.* 2007; Lissaman 1983). However, the performance of such systems is largely determined

by the aerodynamic response of the airfoil to small vortices and gusts in the flow, which are caused by complex building geometries in urban areas added to being a source of flow-induced vibration and noise concern. For that, many researchers have concentrated their efforts on vortex-airfoil interaction problems to investigate the aerodynamic forces operating on the airfoil and assess the system efficiency.

In the literature, different methods for generating the upstream vortex were found: Firstly, when the airfoils go through a localized transverse gust (Perrotta and Jones 2017; Biler *et al.* 2019), secondly, when the airfoils encounter a localized vortex by using numerical vortices models to create the upstream vortical gust (Barnes and Visbal 2018; Zehner *et al.* 2018; Martínez-Muriel and Flores 2020) and finally when the airfoil is placed in the wake of a bluff body (Liao *et al.* 2004; Li *et al.* 2014; Droandi *et al.* 2016). Streitlien *et al.* (1996) investigated the propulsion performances of an airfoil undergoing a pitching and heaving motion placed in front of an upcoming potential vortex flow using the Lagrangian formulation. They found that the phase between foil motion and the arrival of inflow vortices is a critical parameter. Barnes and Visbal (2018) studied vortical-gust interactions with a NACA0012 airfoil operating at a transitional Reynolds number and a counterclockwise-oriented Taylor vortex as the gust. They observed that the intensity, size, and vertical displacement of the vortex with respect to the airfoil affect the times and intensities of previously known maximum lift. At a high Reynolds number, the localized transverse gust is more adapted for hydrodynamic applications. In this case, as demonstrated by Biler *et al.* (2019), the lift and drag coefficients of the wing are dependent on the effective angle of attack during the gust encounter. Furthermore, when the vortex moves downstream, two maximum values of lift coefficient with opposing signs arise as a result of vertical velocity sign changes generated by the vortex on the airfoil. On the other hand, several researchers have used numerical approaches to study the case of an airfoil encountering a localized vortex to evaluate the impact of the incident vortex type on the airfoil's aerodynamic performance. In the same context, Martinez-Muriel and Flores (2020) investigated the vertical gust influence on the NACA0012 airfoil by analyzing both vortex types: the Taylor vortex and the Lamb-Oseen vortex, at a Reynolds number of 1000. According to the authors, the interactions of the airfoil with Taylor and Lamb–Oseen vortices are qualitatively comparable. The airfoil lift coefficient fluctuates, in a non-linear way, with the vertical distance between the vortex and the airfoil at its maximum value roughly proportional to the non-dimensional vortex circulation. However, when the vortex had contact with the airfoil, its instantaneous drag coefficient was negative.

For low Reynolds number, the approach of locating the airfoil in the wake of bluff bodies appears to be more adequate. The experimental setup provides a fundamental understanding of more complex aerodynamic interference problems. Thus, the vortex can be easily defined. In the following, a literature review will be presented on the flow research over cylinders in tandem at low Reynolds numbers to get insight into aerodynamic loads and wake structures.

The arrangement of tandem in-line cylinders is the most studied wake interaction problem in the literature. Zdravkovich (1987) gives a great overview of cylinder interference for a variety of cylinder geometries and the space between them. In laminar flows, Alam *et al.* (2003), demonstrated the effect of fluctuating fluid forces operating on two circular cylinders in tandem. As a result of the downstream cylinder aerodynamics, they noticed that the upstream cylinder mean drag coefficient drops as the pressure distribution along it changes. Huang *et al.* (2012) studied the flow over two rectangular cylinders in tandem at a Reynolds number of 200 for a spacing gap from 1 to 10 using the multi-domain pseudo-spectral approach. They demonstrated that for all gap spacing, the Strouhal number of the two cylinders is the same. Moreover, there is a critical gap for which the downstream cylinder mean drag coefficient increases with a leap from negative to positive. Then, it is progressively reduced when the gap spacing increases). Vakil and Green (2013) performed numerical simulations to study the flow across two circular cylinders in tandem at low Reynolds numbers between 1 and 40. They noticed that as the spacing between the cylinders increases, the normalized drag of the downstream cylinder monotonically approaches unity. Nikfarjam and Sohankar (2015) highlighted the different flow patterns of Power-law fluids through two unconfined square prisms placed in tandem configuration for different spacing ratios for Reynolds numbers of 100 and 150. For a Power-law index of n=0.7 and a Reynolds number of 150, they detected a negative mean drag coefficient of the downstream square cylinder assuming that the spacing gap between them was smaller than 6d (d was the square cylinder side length).

When an airfoil is placed in the wake of a bluff body, an alternation of Van Karman vortices interferes with it. By solving the two-dimensional incompressible Navier–Stokes equations with a Finite Element method, Liao *et al.* (2004) investigated the flow features, the influence of relative position, and the force behavior acting on an airfoil placed in a circular cylinder wake. They recognized that the airfoil vortex shedding frequency was synchronized with that of the cylinder due to its interference. Weiland and Vlachos (2007) focused their experimental setup on the parallel helicopter Blade-Vortex interaction. An active control method based on the Leading-Edge Blowing (LEB) is applied to an airfoil placed in the wake of a circular cylinder. Without applying LEB, the most energetic mode is provided by the vortex shedding of the circular cylinder upstream, according to the POD analysis for the small wake generator. However, the addition of the LEB system reduces the energy contained in this basic mode. Lua *et al.* (2011) investigated the influence of wing-wake interaction on the aerodynamics of a flapping NACA0012 wing. The wing interacts with

its self-generated vortices while making two distinct flapping motions. They reported that the wing-wake interaction can increase or decrease lift force depending on vortex arrangement and flapping wing kinematics. Droandi *et al.* (2016) investigated the effect of a perpendicular vortex on the aerodynamic performances of an oscillating airfoil using both experimental and numerical methods. An airfoil placed upstream of the flapping one created the perpendicular vortex. They observed that an upward velocity component caused by the vortex increased the aerodynamic stress hysteresis acting on the oscillating airfoil. Moreover, the airfoil-vortex interaction produces a loss of performance in terms of the lift coefficient drop when compared to the clean geometry scenario during the down-stroke motion. Peng and Georgy (2017) conducted experimental research on the blade-vortex interaction to study how the small vertical space between them affected the induced fluctuating pressure and noise generated by helicopter blades. A pneumatic system created the vortex by applying a quick pitch motion to an airfoil. They found that the load fluctuation level is affected by both the decay rate of vortex strength and the velocity field near the leading edge of the airfoil at a low Reynolds number. Lefebvre and Jones (2019) experimentally examined the performance of NACA0012 airfoil in the wake of a circular cylinder for various gap distances (x/D). The flow feature characteristics and the aerodynamic performances of the airfoil were determined using the Particle Image Velocimetry (PIV) measuring technique and the load cell sensors. To investigate the interaction phenomena, the Proper Orthogonal Decomposition (POD) approach was used. They established that for all considered cylinder-profile distances (x/D, D being the diameter of the cylinder), the cylinder-airfoil wakes interaction impacts the airfoil performance. For x/D $\leq$ 2, the lift and pitching moment coefficients are significantly small, whereas the drag coefficient is negative. Further, for x/D $\geq$ 3, the aerodynamic coefficients are identical to those of an isolated NACA 0012, but the drag coefficient is negative for $\alpha < 10°$ when x/D < 12.5 and the airfoil does not stall for $0° \leqslant \alpha \leqslant 20°$. Zhang *et al.* (2020) have conducted experimental investigations to study the aerodynamic performances of a stationary wing in the wake of a bluff body. The airfoil is placed at a fixed lateral position and two longitudinal positions were examined for y/c=0 and y/c=-0.7 for different angles of attack. They have concluded that the wing maximum lift coefficient has increased, in comparison to the case when the wing was placed in freestream. It can attain 34% highest value when the wing was placed in the optimum lateral position as well as a delay of the stall angle of 9° was observed. Han *et al.* (2021) have used a numerical tool to study the flow control of a circular cylinder wake by the mean of an oscillating airfoil NACA0012 placed at the centerline of the channel undergoing a pitching motion. They confirmed that the tandem configuration can achieve a more than 50% drag reduction rate. Also, the pitching airfoil can function as a spoiler to control the vortex shedding period.

This research paper examined the performances of the NACA 23015 airfoil placed in a vortical gust flow for low Reynolds number. The influence of the longitudinal and lateral positions, as well as the incoming vortices scale and intensity, was studied. The vortical gust was generated by a square cylinder with a 45° angle of attack placed upstream of the airfoil. A developed numerical tool that solves the stramfunction-vorticity formulation of Navier Stokes equations using the Control-volume-based finite element approach proposed by Saabas and Baliga (1994) was used as well as the Proper Orthogonal Decomposition method was applied to the velocity field to perform an energetic study of the flow feature influenced by the airfoil-vortex interaction.

2. NUMERICAL METHOD

2.1 Governing Equations

The control-volume-based finite element approach is a hybrid of the control volume and the finite element methods that preserve their respective advantages. Many researchers, including Schneider and Raw (1987) and Prakash and Patanker (1985), have developed it.

The stream function-vorticity formulation is used to compute flow characteristics thanks to its numerous advantages in numerical simulations of steady and unsteady flows. The most important benefit is that the pressure term is removed from the governing equations, ensuring that the continuity criterion is automatically satisfied.

During the simulations, the fluid flow is considered to be incompressible, laminar, transient, and two-dimensional with constant physical properties.

The governing equations are written as follows:

- Equation of transport of vorticity:

$$\frac{\partial \omega^*}{\partial t^*} + \left(div\vec{U}\omega^* - \frac{1}{Re}\overrightarrow{grad}(\omega^*) \right) = 0 \quad (1)$$

- Poisson's equation relating the stream function and vorticity:

$$div\left(\overrightarrow{grad}\psi^*\right) = -\omega^* \quad (2)$$

The non-dimensional quantities U(u, v), ω, ψ, p and t, which denote the velocity components, the vorticity, the stream function, the pressure, and the time are respectively used to reduce the number of parameters. They are defined as:

$x = \frac{x^*}{h}$, $y = \frac{y^*}{h}$, $u = \frac{u^*}{u_0}$, $v = \frac{v^*}{u_0}$, $\psi = \frac{\psi^*}{hu_0}$, $\omega = \frac{h}{u_0}\omega^*$, $p = \frac{p^*}{\rho u_0^2}$, $t = \frac{u_0}{h}t^*$

with u_0 and h respectively representing the reference velocity and the reference height. In our case, the reference height h, is equal to the channel height and the reference velocity corresponds to the initial velocity u_0.

After the convergence of stream function and vorticity variables, the pressure term is calculated using Poisson's equation for pressure.

Poisson's equation for pressure is written as follows:

$$div(\overrightarrow{grad}P) = -div\left((\vec{U}.\overrightarrow{grad}).\vec{U}\right) \quad (3)$$

then:

$$div\left(\overrightarrow{grad}P\right) = -2\left(\frac{\partial u}{\partial y}\frac{\partial v}{\partial x} - \frac{\partial u}{\partial x}\frac{\partial v}{\partial y}\right) \quad (4)$$

where P is the pressure.

An unstructured mesh generator based on the Delaunay-Voronoi technique is used to discretize the domain. It has fast grid generation across complex geometries as well as local and adaptive grid refinement capabilities as mentioned in Ben Salah (2006).

The spatial domain is divided into triangular elements with three nodes each. The control volume is formed around each node N by connecting the element centroids Gj to the midpoints M1 and M2 of the respective sides, as illustrated in Fig. 1. Each element has two sides, M1Gj and GjM2; the sub-control volume is bound around N and the control volume (Fig.1b) is built by adding all sub-volumes NM1GjM2N illustrated in Fig. 1(c). The mesh elements are generated one by one from the domain contour data under consideration.

For spatial discretization, an Upwind scheme was adopted based on the neighbor's nodes Nj and Nj+1. The Green-Ostrogradski theorem was applied for the integration of the divergence term. We adopted, then, a linear interpolation function that describes the variation of the stream function, vorticity, and velocity over the triangular element as investigated by Abbassi *et al.* (2003) to evaluate the convection-diffusion flux of the stream function-vorticity formulation. They established that, in the case of a plane channel flow, the linear interpolation function provides more accurate results than the flow-oriented interpolation function. Simpson's rule was used for linear numerical integration.

The conditioned conjugate gradient squared method to solve the discretized equations is frequently used in computational fluid dynamics (CFD) problems.

For the time discretization, an implicit scheme was used. A detailed description of the discretization methodology has been detailed by Ben Salah *et al.* (2005).

2.2 Boundary Conditions

The numerical method adjustment and assumptions were resumed in Table 1 which contains the airfoil, the inlet, the outlet, the channel walls, and the square cylinder side's characteristics.

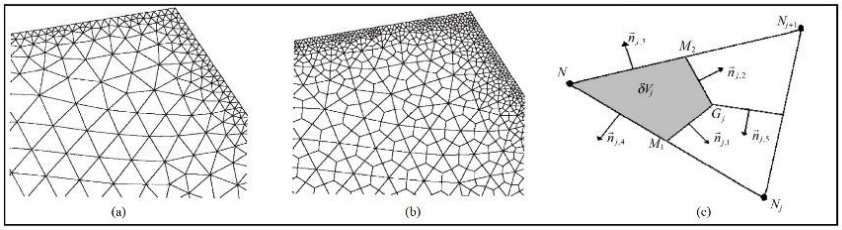

Fig. 1. Unstructured mesh.

Table 1 Boundary conditions

	Velocity	Streamfunction / Vorticity	Pressure
Inlet	• u = cte, depends on the Reynolds number • u = Parabolic profile for the validation case • $v = 0$	• ψ = cte • $\omega = 0$	• P = cte
Outlet	$\begin{cases}\frac{\partial u}{\partial t} + u_{avr}\frac{\partial u}{\partial x} = 0 \\ \frac{\partial v}{\partial t} + u_{avr}\frac{\partial v}{\partial x} = 0\end{cases}$	$\frac{\partial}{\partial t}\left(-\frac{\partial \psi}{\partial y}\right) = u_{avr}\left(\frac{\partial^2 \psi}{\partial x^2} - \omega\right)$	• $\frac{\partial P}{\partial y} = 0$
Solid walls (Channel walls, airfoil, square cylinder)	• $u = v = 0$	ψ = cte	$\begin{cases}\frac{\partial P}{\partial x} = -\frac{1}{\mathrm{Re}}\frac{\partial \omega}{\partial y} \\ \frac{\partial P}{\partial y} = \frac{1}{\mathrm{Re}}\frac{\partial \omega}{\partial x}\end{cases}$

Table 2 Error calculation

Reynolds Number	65	80	100	130	200
Cd (Breuerb *et al.* 2000)	1.46	1.4	1.35	1.32	1.36
Cd (calculated)	1.490	1.416	1.367	1.354	1.422
Error	2.05%	1.14%	1.25%	2.57%	4.55%

For the Outlet, the convective boundary condition was used. According to Abbassi *et al.* (2003), Ol'shanskii and Staroverovon (2000) and Comini *et al.* (1997), the convective boundary condition allows vortical structures to exit outside the boundary without inversed flow, as well as reduces the length of the domain to be examined.

2.3 Lift and Drag Coefficients

In laminar flow, the velocity along the airfoil is decreased by adverse pressure gradients, and the momentum is progressively reduced until separation from the airfoil surface. For that, the laminar flow has less skin friction because of its lower velocity gradient at the surface within the boundary layer. As a consequence, we will focus only on the pressure drag impacts during this study.

The lift and drag coefficients were calculated as follows:

$$C_L = \int_0^1 \left(Cp_{lower} - Cp_{upper}\right) d\left(\frac{x}{c}\right) \quad (5)$$

$$C_D = \int_0^1 \left(Cp_{lower} - Cp_{upper}\right) d\left(\frac{y}{c}\right) \quad (6)$$

2.4 Validation Case

The case of uniform flow past an isolated square cylinder arranged in the channel centerline is examined to assess the accuracy of the numerical method. For various values of Re, the mean pressure drag coefficient C_D is computed and compared to the results of Breuer *et al*. (2000).

As indicated in Fig. 2, the channel length was adjusted to $\frac{L}{D}=50$ with an inflow length of $l=\frac{L}{4}$ and a blockage ratio of 1/8 to reduce the effect of inflow and outflow boundary conditions.

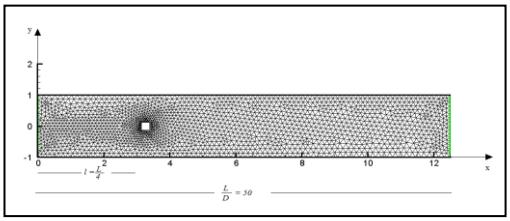

Fig. 2. Unstructured mesh around the square cylinder.

For these simulations, 2008 nodes were used. The inlet velocity profile is considered to be parabolic, with the following equation:

$$u = \frac{3}{2}u_0\left(1-\frac{1}{4}y^2\right), v = 0 \quad (7)$$

The Reynolds number is calculated between 60 and 225 using the velocity u_0 at the centerline of the channel inlet and the square side D as the reference length. During the simulations, the fluid density is set to 1 and the dynamic viscosity is set to $\mu=10^{-4}$.

As shown in Fig. 3, the acquired results were compared to the numerical analysis of Breuer *et al.* (2000). In fact, they are in good agreement, and the difference between the two is less than 5% as illustrated in Table 2.

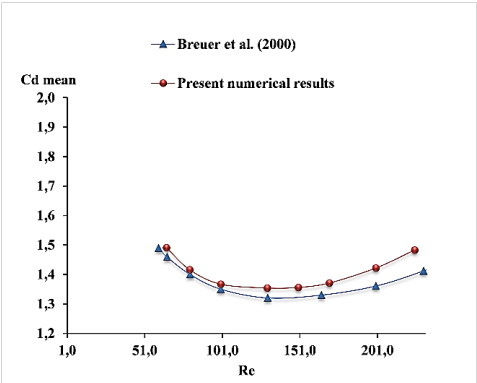

Fig. 3. Comparison of the time-averaged drag coefficient with the results of Breuer *et al.*

3. NUMERICAL RESULTS

This section is structured as follows. The flow characteristics over the asymmetric airfoil NACA23015 at zero angle of attack and the square cylinder at 45° angle of attack with the inflow are first investigated. Second, by modifying the longitudinal and lateral positions of the airfoil, as well as the vortex scale size relative to the airfoil chord length, the influence of the alternating vortex on the airfoil performances is evaluated. Finally, the Proper Orthogonal Decomposition method is used to determine the flow's most energetic structures and to analyze the impingement vortex effects on flow behavior over the airfoil.

3.1 Computational Domain and Preliminary Simulations

The computational domain consists of a plane channel in which the airfoil and the bluff body will be placed at the centerline. It's characterized by a height equal to 2 units and a length L equal to 50xD (50xc in the case of the airfoil) as mentioned in Fig.

3 based on the cylinder diagonal length which is equal to the airfoil chord length of 0.5. The distance between the bluff body and the inlet was respected to *l*=L/4.

Preliminary simulations were necessary to characterize the airfoil performances without vortical flow and determine the airfoil position in the channel.

Firstly, the flow over the NACA23015 airfoil was computed at a 0° angle of attack and a Reynolds number of 500 was calculated based on the chord length equal to 0.5. The domain was composed of 1848 nodes. The axial velocity component of the flow over the airfoil is illustrated in Fig. 4.

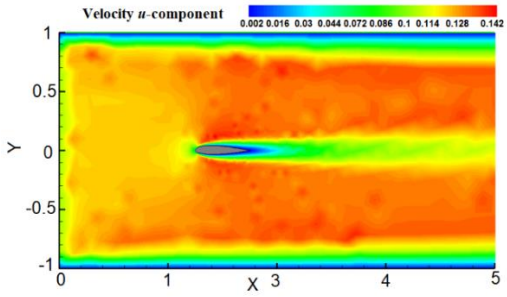

Fig. 4. Axial velocity component « u » of the flow over NACA23015 airfoil at 0° angle of attack and Re=500.

The results show that with a positive pressure upstream, there is no complexity in the flow and no considerable vortex separation. The lift and drag coefficients of the airfoil are both constant and equal to 0.135 and 0.00917 respectively.

As a second step, the wake behind a single square cylinder at a 45° angle of attack for Reynolds number equal to 500, calculated based on the diagonal length of the square cylinder *D*, was examined to determine the positions of the detached vortex in the flow.

A mesh with 1652 nodes was used during the simulations. It was observed that the vortex detachment was periodic, and the Von Karman vortex street was developed. The calculated Strouhal number was equal to 0.208.

The mean flow vorticity is subtracted from the flow field to obtain only the vortex row behind the square cylinder (Fig. 5). It depicts the presence of three distinct regions in the square cylinder wake, designated L1, L2, and L3, respectively, as identified by previous researchers (Roshko 1954; Unal and Rockwell 1988; Lau 2003) as pre-vortex-formation regime (L1), primary-vortex-formation regime (L2), and fully developed-vortex-formation regime (L3). The first zone (L1), depicts the first vortex separation from the square cylinder. As it moves away from the cylinder towards the zones L_2 and L_3, the vortices become fully developed, with a large scale and high circulation.

3.2 Vortex Airfoil Interaction

This section is related to the interaction between the airfoil and the incident vortices. As illustrated in figure 6, the NACA 23015 airfoil with an attack angle of 0°, is placed at the L3 zone for a longitudinal distance G/D equal to 6. During simulations, the Reynolds and Strouhal numbers are calculated using the airfoil chord length, c=0.5, and the inlet velocity as the reference velocity.

At the inlet, a uniform flow in the x-direction of the fluid is prescribed, i.e. u=0.1 and v=0, and the stream function is taken constant equal to 0 in the cylinder and the airfoil walls. For all simulated cases, the physical parameters are taken constant in the initial conditions.

For Reynolds numbers equal to 500, four different meshes were used to test the results independence from grid size: 1675, 1725, 1836, and 1931, respectively. The airfoil pressure mean drag coefficient is summarized in Table 3.

Table 3 Mean drag coefficient for different meshes

Grid number	Mean drag coefficient
1675	-0.0395
1725	-0.0402
1836	-0.0403
1931	-0.0403

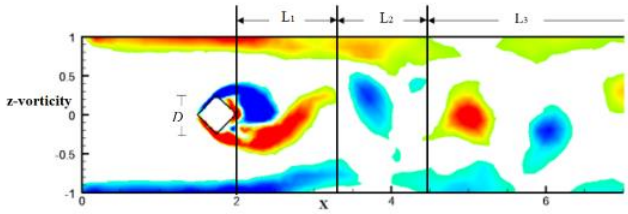

Fig. 5. Row of vortices behind the square cylinder.

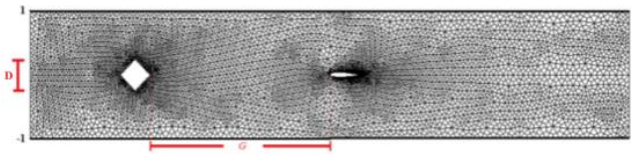

Fig. 6. Unstructured mesh used during the simulations.

The results show that the mean drag coefficient did not vary from 1836 nodes. For that, we opted for a 1931 node mesh in our numerical simulations.

For the time-step independence investigation, three distinct time-steps were examined for a mesh consisting of 1931 nodes: t=0.01s, t=0.001s, and t=0.0001s, respectively. The results demonstrate that from t=0.001s, no changes in the airfoil pressure mean drag coefficient was observed. Thus, we chose this time step to proceed with the simulations.

Figure 7 illustrates the streamlines over four-time steps. The effective angle of attack in front of the airfoil, defined as the angle between the airfoil chord and the velocity vector upstream, becomes unsteady and fluctuating because of a periodic vortex shedding process behind the square cylinder. It denotes the flow local orientation concerning the airfoil leading edge.

Before the shedding process began, the effective angle of attack was 0 (Fig. 7a). Then, it became positive as the shed vortex approached the airfoil (Fig. 7b) and (7c). After that, as the vortex passes over the airfoil, it changes its sign (Fig. 7d).

Considering the upstream vortices' effect on the airfoil, the pressure coefficient changes over time. Figure 8 shows how this phenomenon affects the airfoil aerodynamic coefficients.

Figure 9 exhibits the lift and drag coefficients of the airfoil with time. Due to the presence of an alternating vortex in the flow, the oscillating lift and drag coefficients can be easily seen, affecting both the flow stability and efficiency.

To predict the flow influence on the airfoil performances, spectrum analysis of the airfoil and square cylinder lift force was carried out, as shown in Figure 10. The frequency of vortex separation was estimated using the Fast Fourier Transform (FFT). The sample time is 0.001s, the same as the time step applied in the numerical simulation.

As reported by Liao *et al.* (2004), the airfoil and the square cylinder are detached at the same frequency, indicating that the detachment processes are synchronized.

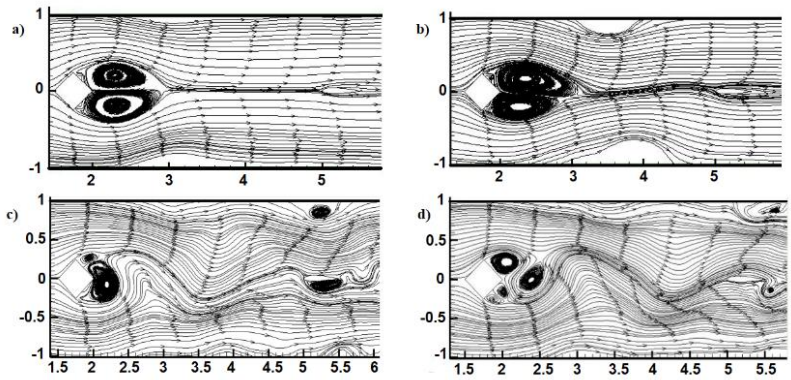

Fig. 7. Streamlines for different time steps.

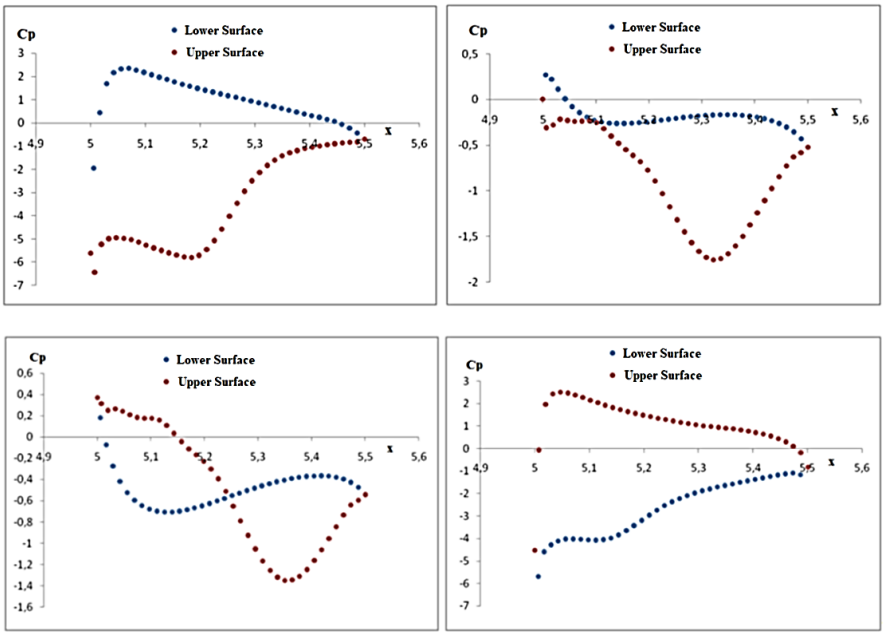

Fig. 8. Pressure coefficient of the airfoil at different time steps ¼ T, ½ T, ¾ T, and T respectively.

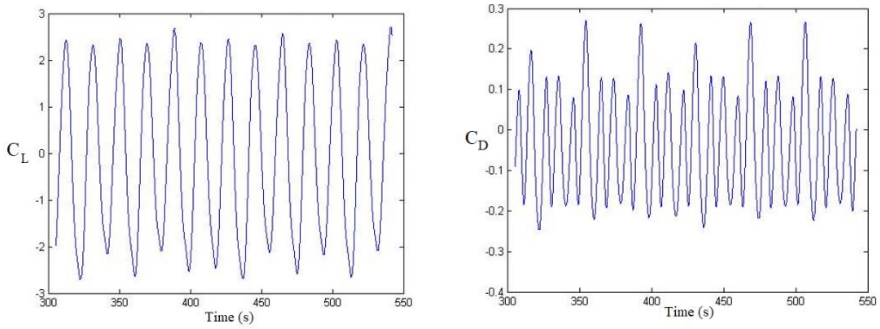

(a) **(b)**

Fig. 9. Instantaneous aerodynamic coefficients of the airfoil: a) lift and b) drag.

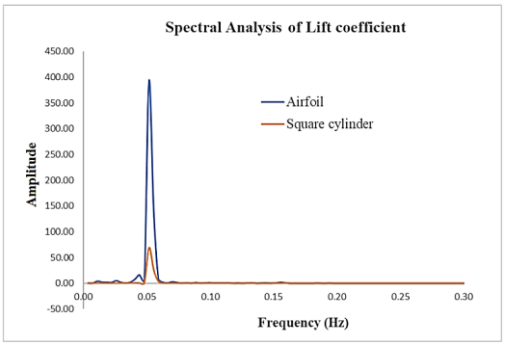

Fig. 10. Amplitude of Power spectral density variation of the airfoil and the cylinder in with frequency.

3.3 Airfoil Position and Vortex Size Effects on the Airfoil Performances

The main geometric parameters that influence the diameter and the intensity of the detached vortices from the square cylinder which are considered as the vortical gust that perturbs the flow are:

- The gap distance between the square cylinder and the airfoil G/D.
- The longitudinal position of the airfoil in respect to the channel centerline T/d.
- The square cylinder diameter in respect to the airfoil chord length D/c.

Table 4 shown below, resumes the simulated cases for the different configurations and Fig. 11 illustrates the geometric parameters.

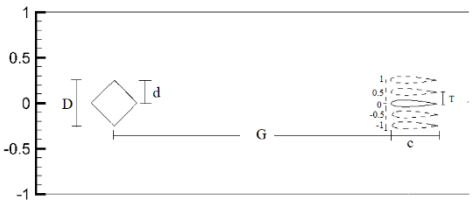

Fig. 11. Geometric parameters that influence the vortical characteristics.

To highlight the longitudinal distance on the airfoil's Strouhal number effect, the airfoil was arranged in zones L2 and L3 in three configurations, G/D = 4, G/D = 5, and G/D = 6 respectively. For each case, Figure 12 represents the evolution of the vorticity field. The primary and fully developed vortices regimes detached from the square cylinder alternately affect the airfoil.

Table 4 The studied Geometric Parameters

Studied cases	Geometric parameters values
Case 1: gap distance G/D (for T/d=0 and D/c=1)	4
	5
	6
Case 2: longitudinal distance T/d (for G/D=6 and D/c =1)	-1
	-0.5
	0
	0.5
	1
Case 3: Cylinder diameter with respect to the airfoil ratio D/c (for G/D=6 and T/d=0)	0.5
	1

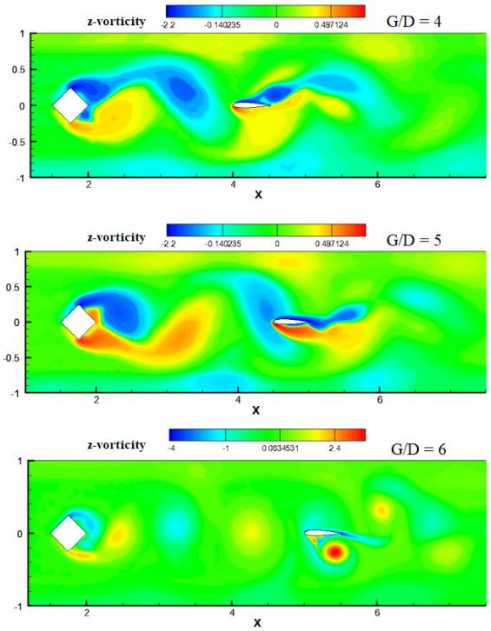

Fig. 12. Vorticity field in the three simulation cases G/D = 4, 5, and 6.

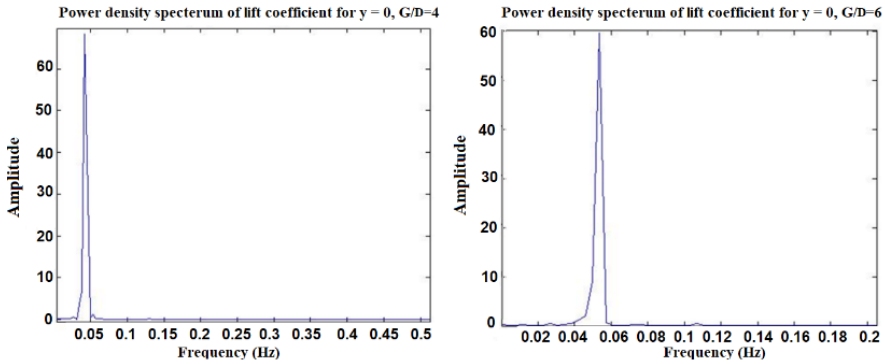

Fig. 13. Power density spectrum of the lift force for the two regions L2 G/D=4 and L3 G/D=6.

In Fig. 13, we can notice that the spectrum contains a peak corresponding to the detachment frequency after applying FFT to the airfoil lift coefficient for various arrangements. As the airfoil approaches the cylinder, the peak lowers, and the minimal Strouhal number is reached. In the L2 position for G / D = 4, the Strouhal number is roughly 0.215, which is close to the vortex shedding frequency of a single cylinder (St ≈ 0.2). It rises to approximately 0.267 for the L3 regime when the airfoil is farther than the cylinder, due to a decrease in the intensity of fully developed vortices during flow convection.

The selected four lateral locations of the airfoil, for G/D = 6, were illustrated in Fig. 14. They are characterized by a T/d ratio where T is the vertical position of the airfoil with respect to the channel centerline and d is the half square diagonal length. The simulations were performed for the cases T/d = -1, -0.5, 0, 0.5, and 1, respectively to investigate the airfoil lateral positions' impact on its aerodynamic performances.

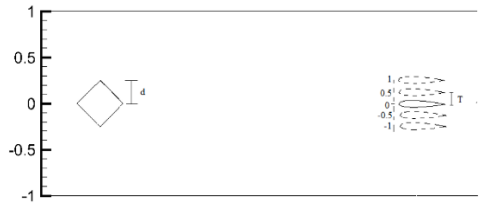

Fig. 14. Different lateral positions of the airfoil.

Figure 15 shows the streamlines and the vorticity fields for the different positions.

In fact, for T/d = 1, 0.5, and 0, the vortices divide and interfere with the shear layer formed on the airfoil upper surface. However, For T/d= -0.5, and -1, the vortices pass smoothly from the upper surface and approach the airfoil leading edge. After analyzing the instantaneous lift and drag coefficients for the various positions, the same coefficient behavior was observed between T/d = 1 and -1 and T/d = 0.5 and -0.5. Figure 16 will only show the time history of the lift and drag coefficients for T/d values of -0.5 and -1.

In comparison with the position of T/d =0 shown in

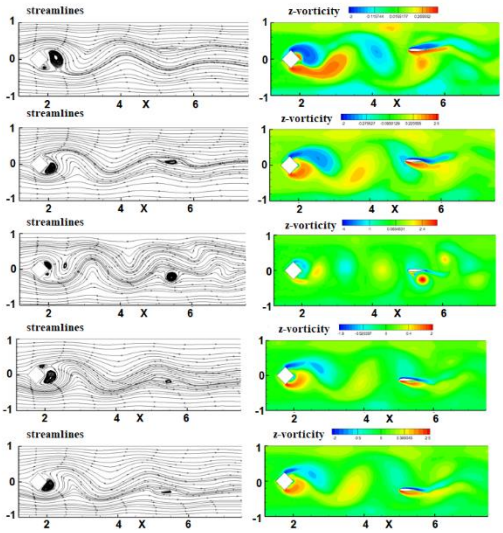

Fig. 15. Streamlines and vorticity field of the flow for the different airfoil positions.

Figure 11, as T/d grows, the maximum value of CL drops. In addition, the influence of T/d on the drag coefficient of the airfoil (Fig. 16b) demonstrates that increasing T/d causes a rise in drag. This phenomenon is most probably caused by a change in the effective attack angle combined with an increase in the pressure drag due to the small gap between the channel wall and the lower surface of the airfoil. Thus, the intensity of the suction peak at the airfoil leading edge is reduced and a flow acceleration is observed because of the additional horizontal velocity induced by the vortex on the airfoil. The findings agree with those of Martnez-Muriel and Flores (2020), who found an increase in the airfoil drag coefficient at T/d =-1.

In comparison with the values obtained for different lateral positions in Fig. 17, the mean drag coefficient is negative at the channel centerline for T / d = 0. The development of negative mean drag coefficients is mostly caused by the shielding effects from the upstream cylinder due to the presence of low-pressure distribution, as well as a well-developed stable vortex structure in the space between the two cylinders, as Tang *et al.* (2015) demonstrated.

Furthermore, the experimental investigation of Lefebvre and Jones (2019) proves that the negative

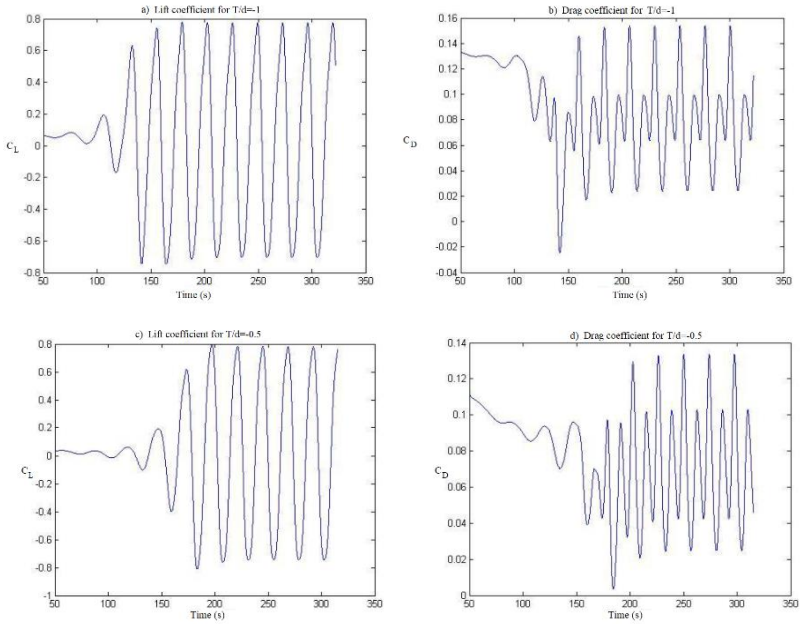

Fig. 16. Instantaneous lift and drag coefficients of the airfoil for T/d =-0.5 and -1 respectively.

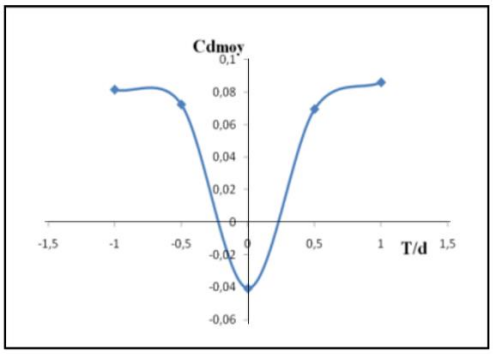

Fig. 17. Variation of the mean drag coefficient with the lateral position T/d.

mean drag coefficient on the airfoil can be identified for angles of attack $\alpha \leq 10°$ and a distance gap can reach x/D=12.5 considering that the stall phenomenon cannot be observed for this range of attack angles. For that, the pressure contours in the flow field are depicted in Fig. 18 for a gap distance G/D= 6 and T/d= 0 where the solid lines correspond to positive pressure since the dashed lines indicate a negative pressure. It reveals the presence of a low pressure and fully developed stable vortices in the region between the cylinder and the airfoil.

The airfoil generates thrust in this condition, as indicated by the negative mean drag coefficient which keeps rising and becomes positive as the airfoil approaches the channel walls, creating a drag force.

The variation of the Strouhal number with the airfoil lateral position is shown in Figure 19 to examine the influence of the perturbed flow on the airfoil shed frequency for each position (T/d). The frequencies are calculated using an FFT analysis of the airfoil lift coefficient. In fact, this illustrates that when the airfoil is placed at T/d= 0, the Strouhal number reaches its maximum and then reduces since the airfoil moves further from the center.

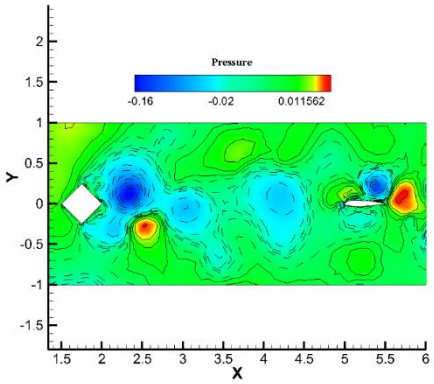

Fig. 18. Pressure contour in the gap between the square cylinder and the airfoil.

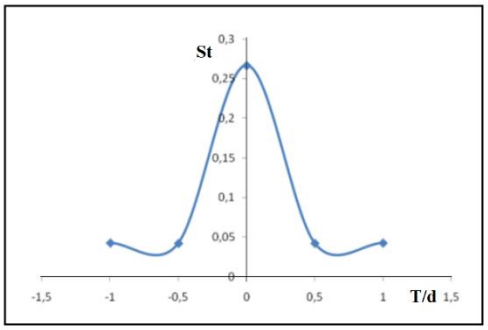

Fig. 19. Strouhal number for lateral positions T/d =-1, 0.5, 0, 0.5 and 1 respectively.

The impingement core vortex scale size is then investigated. Their size is changed by reducing the

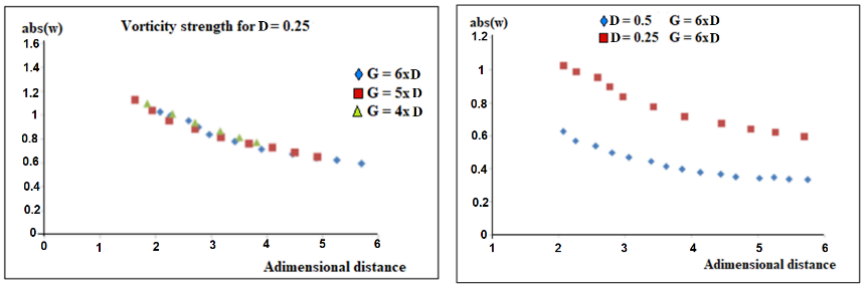

Fig. 20. Variation of the vorticity intensity in the incident core vortex a) for d=0.25 G/D=4, G/D=5, and G/D=6, b) case of d=0.25 and d=0.5 avec G/D=6.

diagonal square cylinder length while maintaining the airfoil chord length fixed at c=0.5. For a diagonal length of d = 1/2 × c and d = c, comparative research will be conducted to determine the effect of vortex size on the lift coefficient of the airfoil.

Figure 20 shows the maximum absolute value variation of vorticity for each x position when d = c and d = 1/2 × c for the different values of G/D.

As the core vortex reaches the airfoil, the intensity of the vortex drops. Further, because a vortex's tangential velocity is inversely related to its radius, its intensities grow as the diameter of these vortices is reduced.

The size of the vortex affects the airfoil's aerodynamic performance, particularly the lift coefficient, as in Fig. 21 when the vortex emerges from the square cylinder and continues through the flow until it reaches the airfoil. The x-axis represents the vortex's non-dimensional position in the flow field before it touches the airfoil, normalized by the square diagonal d.

As shown in Fig. 20b, the peak values of the lift coefficient increase as the diameter of the core vortex grows due to decreased vorticity. Martnez-Muriel and Flores (2020) reported the same outcome while exploring the large gust vortical effect on airfoil performance.

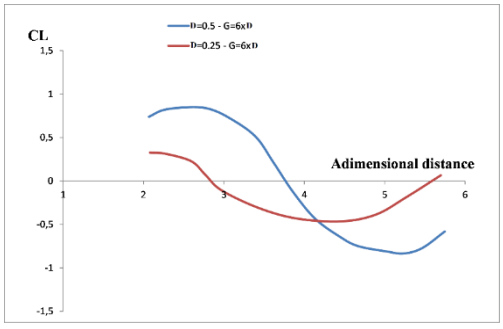

Fig. 21. Variation of the airfoil lift coefficient with the longitudinal distance for D=0.25 and D=0.5 G/D=6 case.

4 PROPER ORTHOGONAL DECOMPOSITION ANALYSIS

The Proper Orthogonal Decomposition (POD) method based on the snapshot technique detailed by Sirovich (1987), was used in this study. Its main concept is to find a set of orthogonal functions or Eigen modes saved in energy content descending order, with the dominant ones expressing the flow-defining characteristics.

The snapshot approach entails expressing the investigated functions *f(x)* in terms of Eigenmodes that are dependent on the snapshot:

$$f_n(x) = \sum_{n=1}^{K} \left(a_n \Phi_n(x) \right) \tag{8}$$

with $f_n(x) = f(x, nt)$ is the instantaneous velocity field of snapshots and K is their total number.
Since the Eigen modes $\Phi_n(x)$ are orthonormal, the respective coefficients modes are uncorrelated as:

$$\langle a_n a_m \rangle = \lambda_n \delta_{nm} \tag{9}$$

Here the operator $\langle \cdot \rangle$ denotes ensemble average. The eigenvalue λ_n represents the contribution of the corresponding Eigen modes $\Phi_n(x)$ to the total energy. These are expressed as follow according to Bastine et al. (2014):

$$\Phi_n(x) = \sum_{n=1}^{K} \left(\zeta_n f_n(x) \right) \tag{10}$$

where the coefficients ζ_n are the eigenvectors of the spatial correlation matrix C given by the velocity fields inner product at times n and m:

$$C_{nm} = \frac{1}{N} (f_n, f_m) \tag{11}$$

It is important to note that POD is a mathematical framework and the correlation operator Eigen functions are associated with coherent structures based on interpretation and fluid dynamical understanding.

The POD approach was applied in this work to determine the most energetic structure and its contribution to the overall flow. With varied spacing ratios, the POD analysis was conducted using the velocity field variable and the airfoil at a 0° angle of attack for a Reynolds number equal to 500. The first ten eigenvalues are analyzed to determine the method sensitivity to the number of snapshots K. The gap between the cylinder and the airfoil is equal to G/D=6, and the airfoil is situated at the channel centerline (T/d=0) in this case. The results show that when the number of snapshots is greater than 85, the

magnitude of the greatest values does not change considerably.

Furthermore, Mula and Tinney (2014) and Dahmouni *et al.* (2017) both indicated that kinetic energy is commonly adopted as a convergence criterion for the POD Snapshot method. The reduced-order POD model obtained can be utilized to reconstruct a velocity map with the majority of details that characterize flow behavior. For this purpose, the energy contents of the first four energetic modes are shown in Fig. 22 for various numbers of snapshots. For a set of snapshots greater than or equal to 85, it is obvious that the energy content of POD modes does not change significantly.

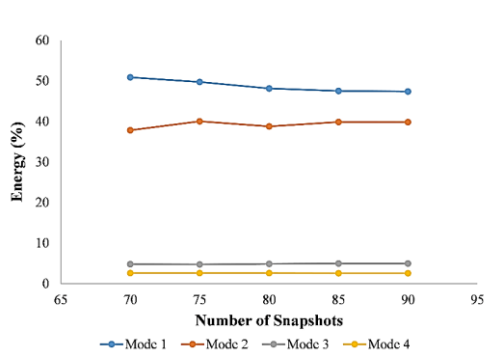

Fig. 22. Energy of the first four POD modes for different snapshots.

4.1 POD Energetic Analysis

For various G/D, T/d, and D/c configurations, the POD approach was used. A total of 400 snapshot samples were used in the following analysis. For each scenario, the energy contribution contained in the Ten first energetic modes versus the number of POD modes is shown in Fig. 23.

The high energy content of the first two POD modes is the first observation. When the airfoil is placed at the channel centerline with G/D= 6 and T/d= 0, they contain 87 percent of the fluctuating vortices' total energy in the wake. In addition, it can reach higher values greater than 90% in situations T/d=0.5 and 1. Then, the energy content of the successive Eigenmodes rapidly drops for the second pair mode (3^{rd} and 4^{th} modes together). Its maximum value was roughly 11 percent for T/d= -1. The main energy in the first-order POD mode (modes 1 and 2) reveals the periodic character of the detached vortices process.

Figure 24 shows the POD temporal coefficients in the form of phase portraits, often known as Lissajous curves, as a function of the first mode coefficient for the case G/D= 6 and T/d= 0. This diagram depicts the signal's quasi-periodic nature (the curves are closed) as well as the increase in the characteristic frequency observed from one pair to the next. The lobes in the phase portraits correspond to the velocity coefficients harmonic.

The coefficient a2=f(a1) is illustrated in Fig. 24 a), which shows that the Lissajous line of the first two modes forms an ellipse, implying that the modes describe an oscillating process and that the first two ones have the same frequency. In fact, the infinity-like shape of the modal pair between a1 and a4 (Fig. 24 b) demonstrates that the second mode-pair is the second harmonics with respect to the first, as described by Samani (2014) and Oberleithner *et al.* (2011).

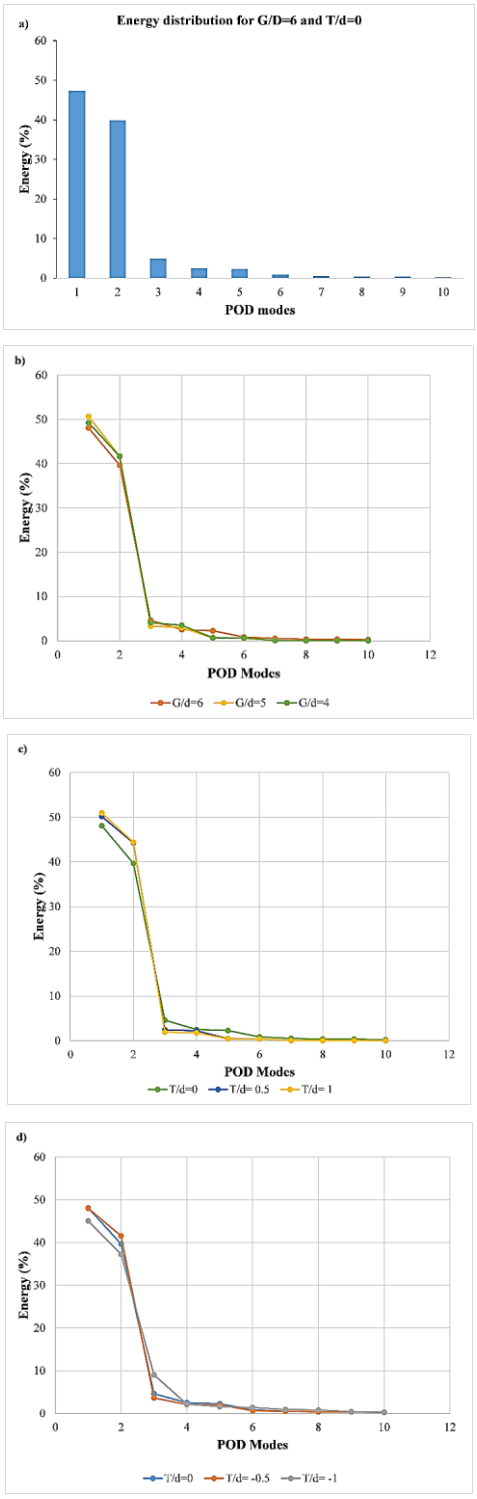

Fig. 23. Energy distribution of the first 10 POD modes: a) case G/D=6, b) cases G/D=4, 5 and 6, c) cases T/d=0, 0.5 and 1, d) cases T/d=0, -0.5, and -1 respectively.

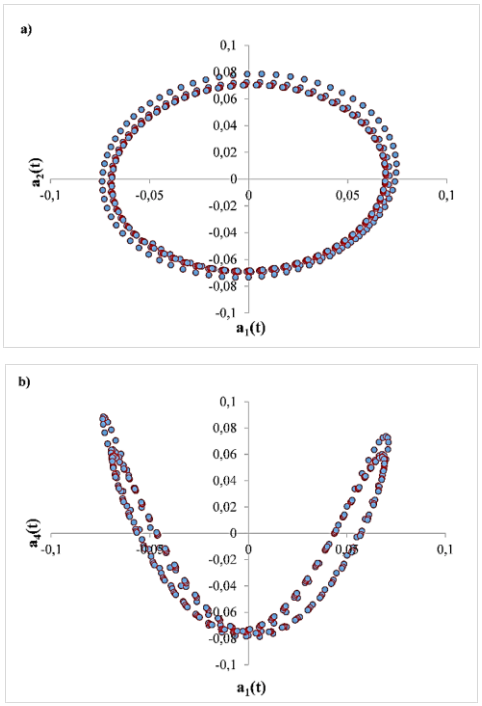

Fig. 24. Lissajous curves of the temporal coefficients of the POD modes: a) $a_2(t) = f(a_1)$, b) $a_4(t) = f(a_1)$.

4.2 POD Vorticity Fields

The first two normalized POD Eigenmodes referring to the fluctuating velocity components of the axial velocity are illustrated in Figs. 25 and 26 for better explaining the behavior of the most energetic coherent structure in the flow. The first two modes have a similar pattern, consisting of alternated large-scale spatial structures, and show how the wake structures are periodic and convective.

The vorticity field of POD modes 3 and 4 are presented in Fig. 27. Mode 3 shows two parallel rows of half-arrowhead structures which are antisymmetric about the centerline, indicating that this mode is associated with symmetrical vortex shedding from the square cylinder, as studied by Leite *et al.* (2018), and Wang and Lam (2019). The fourth POD mode depicts an antisymmetric shedding process by arranging small alternated vortices symmetric about the centerline as observed in cases of modes 1 and 2. The results show that there are two types of vortex shedding processes: symmetric and antisymmetric.

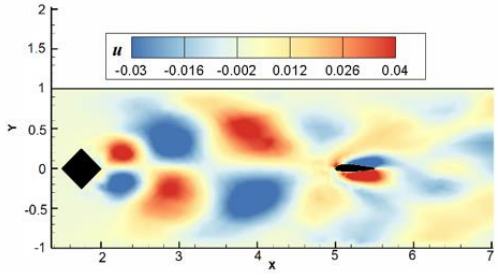

Fig. 25. 1st POD mode of the *u*-component of the fluctuating velocity for the case G/D=6 and T/d=0.

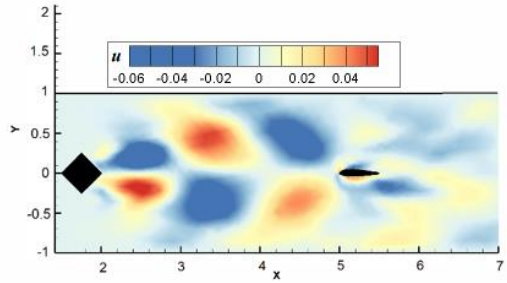

Fig. 26. 2nd POD mode of *u*-component of the fluctuating velocity for the case G/D=6 and T/d=0.

The vorticity field of the first four POD modes of the cases T/d= 1 and the case D/c=0.5 for G/D= 6 are presented in figures 28 and 29 respectively.

Large-scale flow structures dominate the flow in all the simulated cases for the first two modes, explaining why they contain the highest energy content in the flow and denote the vortex shedding process. It can be observed also that as the order of modes grows, the vortex structure changes from large to small scales, corresponding to a gradual decrease in vortex energy.

When the vortex scale size is reduced corresponding to D/c=0.5, POD analysis yields the same flow pattern. Figure 29 depicts the vorticity field of the first four POD modes with G/D=6 and T/d=0.

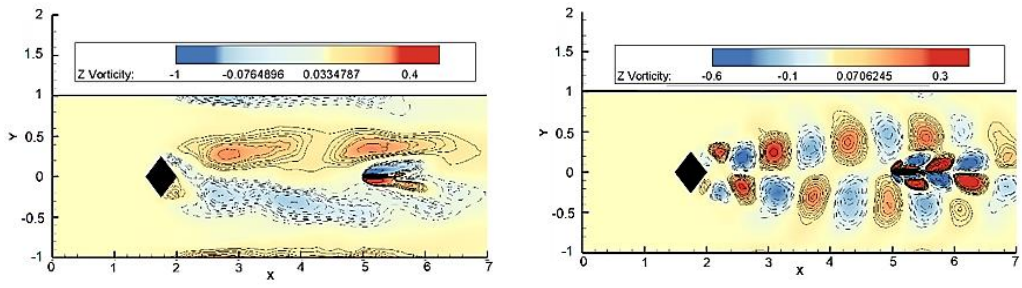

(a) (b)

Fig. 27. Fluctuating vorticity field of the 3rd and 4th POD modes for the case G/D= 6 and T/d=0: a) mode 3 and b) mode 4.

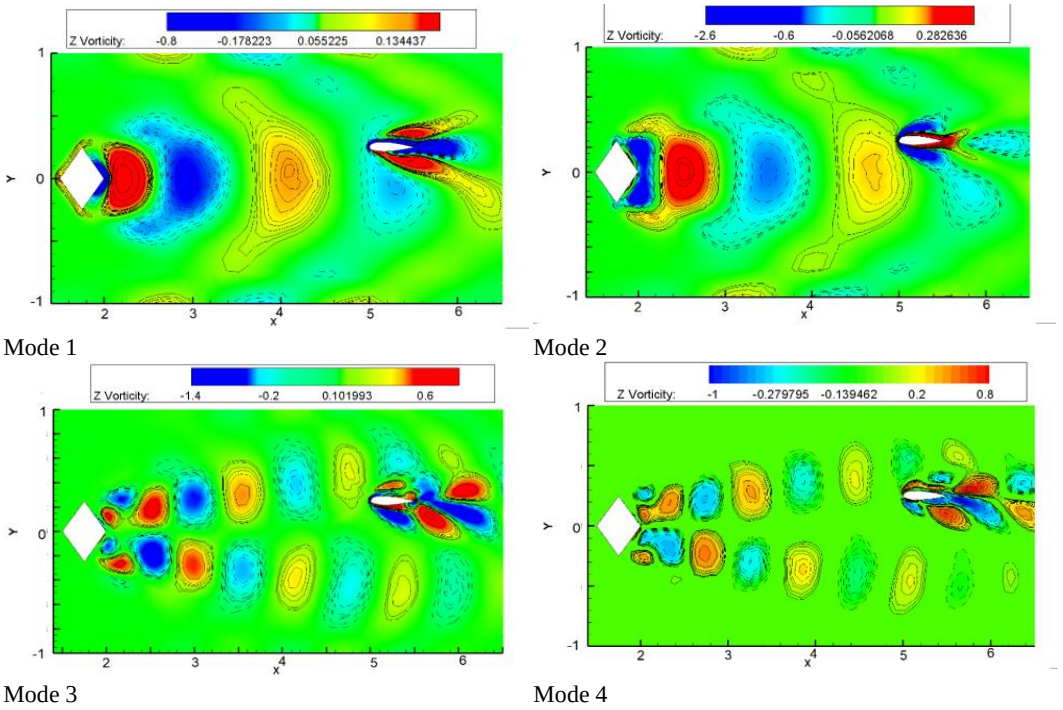

Mode 1 Mode 2

Mode 3 Mode 4

Fig. 28. Vorticity of the four first POD modes for G/D=6 and T/d =1.

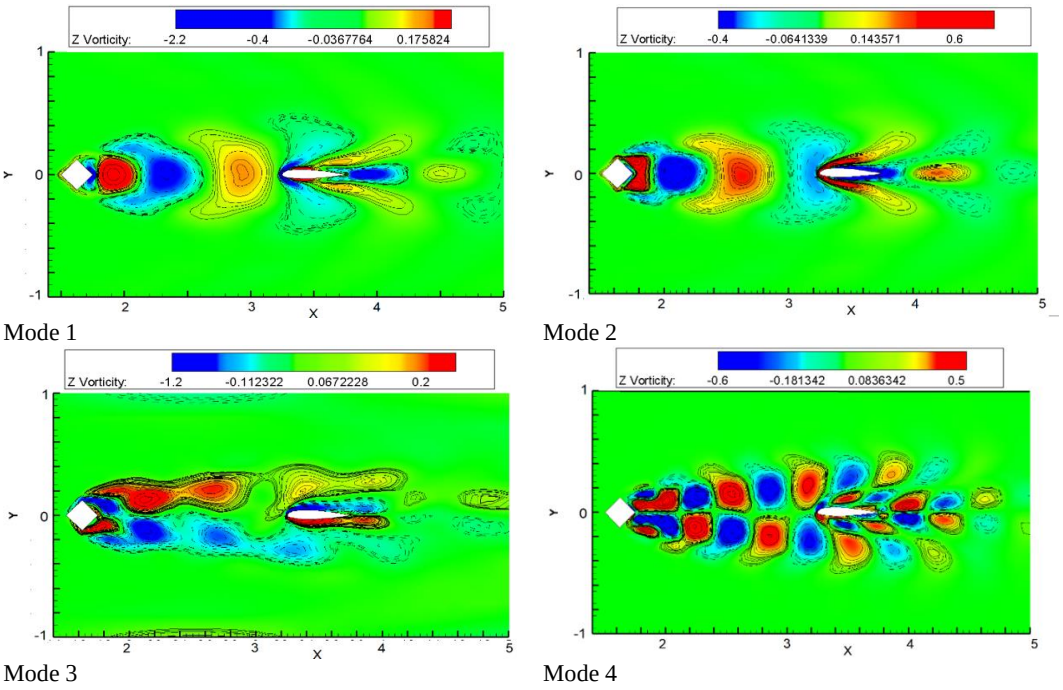

Mode 1 Mode 2

Mode 3 Mode 4

Fig. 29. Vorticity of the four first POD modes for G/D=6, T/d =0, and D/c= 0.5.

4.3 POD Analysis Near the Airfoil

The first two POD modes of the fluctuating velocity components *u* and *v* are shown in Figs. 30 and 31, respectively, to study the effect of impingement vortices on the airfoil detachment process.

The u-component of the fluctuating velocities of the first two modes depicts a quadripole around the airfoil, indicating that an elliptical deformation of the vortex core occurred by raising the base-flow vorticity in one direction while decreasing it in the perpendicular direction. Whereas, the *v*-components of the first two modes illustrate the elongation and compression of the impingement vortex in front of the airfoil.

As demonstrated in Figures 32 and 33, modes three and four depict the interaction between the airfoil and the vortices in the flow. Mode three exhibits the detachment of double core vortices from the airfoil

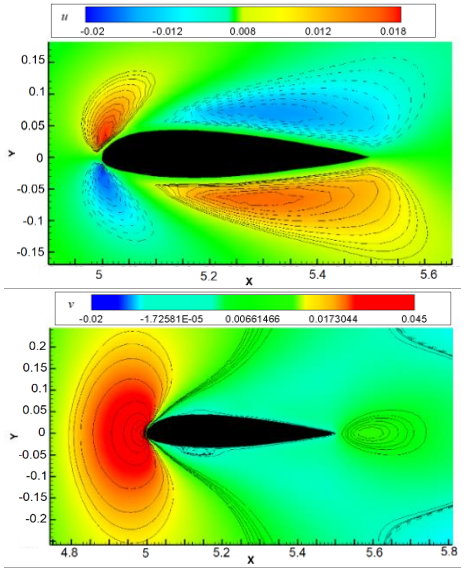

Fig. 30. The u and v components of the fluctuating velocity of the 1st POD mode.

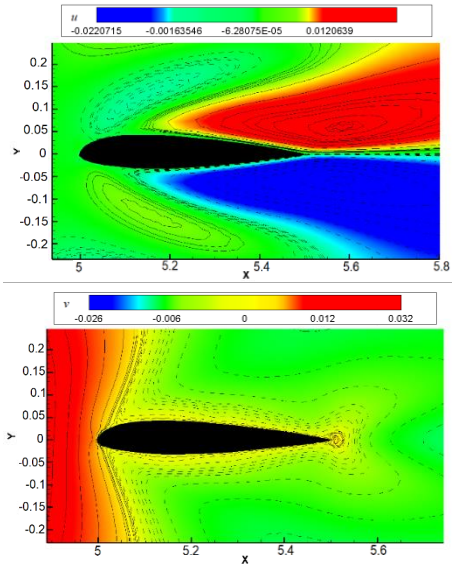

Fig. 31. The u and v components of the fluctuating velocity of the 2nd POD mode.

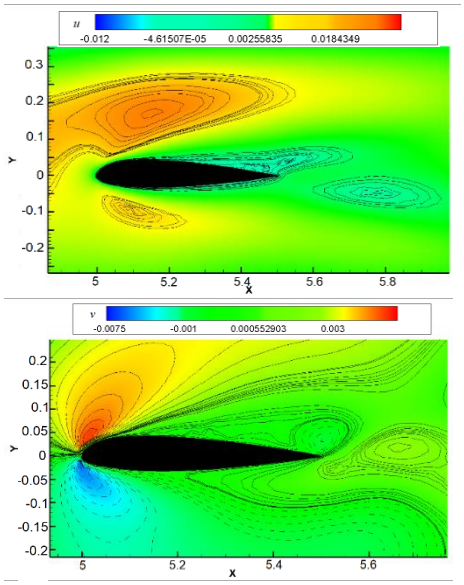

Fig. 32. The u and v components of the fluctuating velocity of the 3rd POD mode.

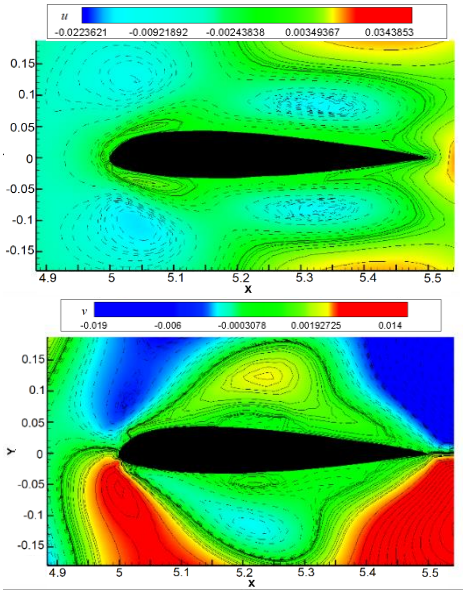

Fig. 33. The u and v components of the fluctuating velocity of the 4th POD mode.

trailing edge into the wake, while mode four displays the decomposition of flow vortices into small vortices bounded to the leading edge and on the upper and lower surfaces of the airfoil.

4.4 Spectral Analysis

To highlight the effect of the vortices in the flow on the airfoil detachment frequency as a function of airfoil location, spectrum analysis is required. For all simulated cases, the temporal coefficients of the first two POD modes, a1 and a2, are treated using the FFT. As demonstrated in Fig. 34 for the cases G/D= 5, T/d=0, and D/c= 1, they have the same frequency for all spacing ratios and gap distances. This allows us to just concentrate the spectral analysis on the temporal coefficient of the first POD mode.

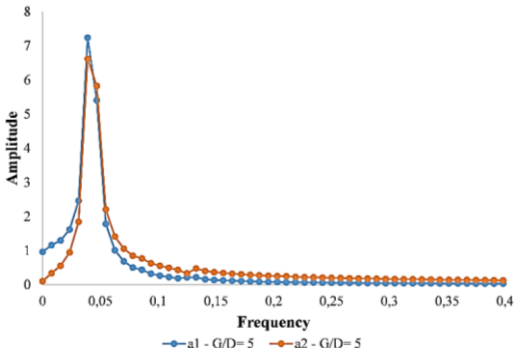

Fig. 34. Amplitude of FFT of the temporal coefficients a1(t) and a2(t) of the first two POD modes for the case G/D= 5, T/d=0, and D/c= 1.

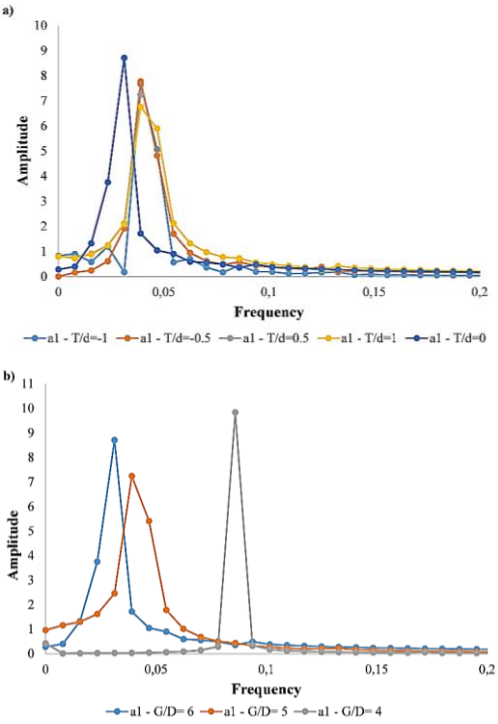

Fig. 35. Amplitude of FFT of the temporal coefficient a1(t) of the 1st POD mode: a) T/d=-1, -0.5, 0.5 and 1 for G/D= 6. b) for G/D= 4, 5 and 6 for T/d= 0.

In fact, for D/c =1, the FFT of the temporal coefficient a1(t) is calculated and presented in figure 35 for various spacing ratios and gap distances.

The frequency of the dominating modes (mode 1 and mode 2) does not change for all cases, as shown in Figure 35a). The results show that the different variations in the lateral position of the airfoil do not affect the frequency of vortex shedding. Despite that, the frequency rises with respect to T/d=0.

By analyzing the effect of the gap distance, it is clear in Figure 35b) that when the gap distance between the airfoil and the square cylinder G/D grows from 4 to 6, the frequency of the temporal coefficient is affected and dropped. Table 5 summarizes the different frequency values as a function of G/D.

Table 5 Frequency of a1(t) for different gap distance G/D= 4, 5 and 6

Position	Frequency
G/D = 4	0.0859
G/D = 5	0.0390
G/D = 6	0.0312

We can deduce that the gap distance G/D has a significant impact on the vortex shedding frequency. Furthermore, as shown in Fig. 36, when comparing the two cases D/c= 1 and D/c = 0.5 for the same gap distance G/D= 6 and T/d=0 position, the vortex size is, indeed, an essential factor that influences the vortex shedding frequency.

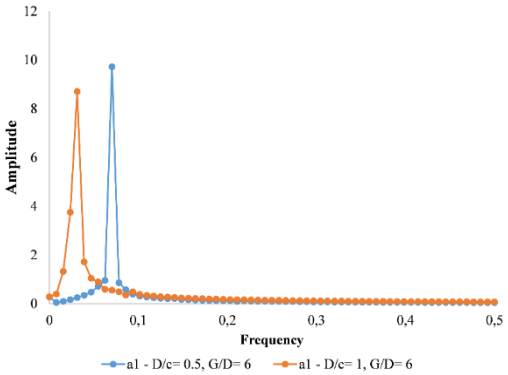

Fig. 36. Amplitude of FFT of the temporal coefficient a1(t) of the 1st POD mode for D/c=0.5 and D/c= 1.

5. CONCLUSION

In this paper, the vortex-airfoil interaction phenomenon has been investigated. The flow behavior and aerodynamic properties of the NACA23015 airfoil in a perturbed flow for low Reynolds numbers were numerically investigated. Using the Control-volume-based finite element approach, a homemade numerical tool was developed to solve the Navier Stokes equations' stream function-vorticity formulation (CVFEM). A 45° angle of attack square cylinder placed at the channel inlet was used to generate upstream vortices. The existence of vortices in the flow causes an unstable effective angle of attack in front of the airfoil. These changes in the flow features modify the vortex detachment process from the airfoil and synchronize its vortex detachment frequency with the square cylinder one. As a consequence, the pressure coefficient and the aerodynamic coefficients (lift and drag) of the airfoil change over time and their behavior depends on the airfoil position regarding the cylinder and the vortices scales.

The Strouhal number of the airfoil was closer to the vortex shedding frequency of a single cylinder for low gap distance between them and increased when the longitudinal distance growth about 0.267 for G/D =6 due to the decrease of the fully developed vortices intensity during convection in the flow. In addition, when increasing the lateral position of the airfoil (T/d) from the centerline of the channel, the maximum values of the lift coefficient C_L decrease in comparison with the case of T/d =0, and an increase of the mean drag coefficient is observed. For T/d =0, a negative mean drag coefficient is observed due to the existence of low-pressure distribution, together with a well-developed stable vortex structure in the gap between the airfoil and the square cylinder. Moreover, the effect of the scale size of the impingement core vortex has a particular impact on the lift coefficient illustrated by an increase of its peak values when increasing the core vortex diameter due to the vorticity decrease.

Finally, the Proper Orthogonal Decomposition technique was applied to analyze the flow feature

and the impact of the impingement vortices on the airfoil. The first two modes contain together 87% of the total kinetic energy of the flow and attain its maximum for the cases T/d=1. The Lissajous curves indicate that the first two modes describe an oscillating process and have the same frequency. The second mode-pair is the second harmonics with respect to the first one. The vorticity analyses of the POD modes for the different gap distance G/D and different ratios T/d demonstrate the existence of two types of vortex shedding process: symmetric and antisymmetric. Also, the importance of the symmetric shedding vortex mechanism depends on the distance ratio T/d. Near the airfoil, the POD modes give information on how the impingement airfoil and the upstream vortices interact. In fact, the first pair of POD modes illustrate an elliptical deformation of the vortex core over the airfoil in the *u*-component, whereas the *v*-component proves the elongation and compression of the impingement vortex in front of the airfoil leading edge. Also, the second pair of POD modes (modes three and four) highlights the interaction phenomenon between the vortices in the upstream flow and the airfoil. The 3rd mode validates the impact of this interaction on the detachment process from the trailing edge of the airfoil in terms of double core vortices, and mode four illustrates the division into small vortices bounded to the leading edge and on the upper and lower surfaces of the airfoil. Finally, the spectral analysis of the temporal coefficient of the first mode specifies that the shedding vortex frequencies are not affected by the distance ratio T/d= -1, -0.5, 0.5, and 1 respectively. It depends mainly on the gap distance between the airfoil and square cylinder G/D as well as on the scale size of the upstream vortices.

IN MEMORY OF PROFESSOR SASSI BEN NASRALLAH

We would like to pay tribute to our dear Professor Sassi BEN NASRALLAH, who contributed to the numerical code elaboration before his sudden death in June 2017. Professor Sassi BEN NASRALLAH was for us an excellent teacher, a serious person, and a scientific luminary. We lost more than just a colleague, but a scientific father.

REFERENCES

Abbassi, H., S. Turki and S. Ben Nasrallah (2003) Interpolation functions in control volume finite element method. *Computational Mechanics* 30, 303-309.

Alam, M. M., M. Moriya, K. Takai and H. Sakamoto (2003). Fluctuating Fluid Forces Acting on Two Circular Cylinders in a Tandem Arrangement at a Subcritical Reynolds Number. *Journal of Wind Engineering and Industrial Aerodynamics* 91, 139–154.

Barnes, C. J. and M. R. Visbal (2018). Counterclockwise vortical-gust/airfoil interactions at a transitional Reynolds number. *American Institute of Aeronautics and Astronautics Journal* 56(7), 2540–2552.

Bastine, D., B. Witha, M. Wächter and J. Peinke (2014). POD analysis of a wind turbine wake in a turbulent atmospheric boundary layer. *Journal of Physics: Conference Series* 524(1), 012153.

Ben Salah, M. (2006). *Contribution à resolution des problems des transferts couples de chaleur par les method des volumes finis*. Ph. D. thesis, National of Engineering School of Monastir, University of Monastir, Monastir, Tunisia.

Ben Salah, M., F. Askri and S. Ben Nasrallah (2005). Unstructured Control-Volume Finite-Element Method for Radiative Heat Transfer in a Complex 2-D Geometry. *Numerical Heat Transfer, Part B: Fundamentals: An International Journal of Computation and Methodology* 48(5), 477-497.

Biler, H., C. Badrya and A. R. Jones (2019). Experimental and computational investigation of transverse gust encounters. *American Institute of Aeronautics and Astronautics Journal* 57, 1–15.

Breuer, M., J. Bernsdorf, T. Zeiser and F. Durst (2000). Accurate computations of the laminar fow past a square cylinder based on two different methods: lattice-Boltzmann and finite-volume. *International Journal of Heat and Fluid Flow* 21, 186-196.

Comini, G., M. Manzan and G. Cortella (1997). Open boundary conditions for the steamfunction-Vorticity formulation of unsteady laminar convection. Numerical Heat Transfer, Part B 31, 217.

Dahmouni A. W., M. M. Oueslati, S. Ben Nasrallah (2017). Experimental Investigation of Tip Vortex Meandering in the Near Wake of a Horizontal-Axis Wind Turbine. *Journal of Applied Fluid Mechanics* 10(6), 1679-1688.

Droandi, G., G. Gibertini and A. Zanotti (2016). Perpendicular blade–vortex-interaction over an oscillating airfoil in light dynamic stall. *Journal of Fluid and Structures* 65, 472–494.

Han, R., W. Liu, X. L. Yang and X. H Chang (2021). Effect of NACA0012 Airfoil Pitching Oscillation on Flow Past a Cylinder. *Energies* 14, 5582.

Huang, Z., G. Xi and W. Zhang (2012). Numerical simulation of spacing effects on the flow past two 2:1 rectangular cylinders in tandem at Re = 200. *In proceedings of ASME Fluids Engineering Division Summer Meeting collocated with the ASME Heat Transfer Summer Conference*, Rio Grande, Puerto Rico, USA, 1007-1015.

Lau, Y. (2003). *Experimental and Numerical Studies of Fluid-Structure Interaction in Flow-Induced Vibration Problems*. Ph. D. thesis, The Hong Kong Polytechnic University, Hong Kong, China.

Lefebvre, J. N. and A. R. Jones (2019). Experimental Investigation of Airfoil Performance in the Wake of a Circular Cylinder. *American Institute of Aeronautics and Astronautics Journal* 57(7), 2808-2818.

Leite, H. F., A. C. Avelar, L. Abreu, D. Schuch and A. Cavalieri (2018). Proper orthogonal decomposition and spectral analysis of a wall-mounted square cylinder wake. *Journal of Aerospace Technolgy and Management* 10, e2118.

Li, Y., X. N. Wang, Z-W. Chen and Z. C. Li (2014). Experimental study of vortex–structure interaction noise radiated from rod–airfoil configurations. *Journal of Fluid and Structures* 51(4), 313-325.

Liao, Q., G. J. Dong and X. Y. Lu (2004). Vortex formation and force characteristics of a foil in the wake of a circular cylinder. *Journal of Fluid and Structures* 19(4), 491-510.

Lissaman, P. B. S. (1983). Low-Reynolds number airfoils. *Annual Review of Fluid Mechanics* 15, 223-239.

Lua, K. B., T. T. Lim and K. S. Yeo (2011). Effect of Wing-Wake Interaction on Aerodynamic Force Generation on a 2D Flapping Wing. *Experiments in Fluids* 51(1), 177–195.

Martínez, M. C. and O. Flores (2020). Analysis of vortical gust impact on airfoils at low Reynolds number. *Journal of Fluid and Structures* 99, 103138.

Mueller, T. J. and J. D. DeLaurier (2003). Aerodynamics of small vehicles. *Annual Review of Fluid Mechanics* 35, 89-111.

Mueller, T. J., J. C. Kellogg, P. G. Ifju and S. Shkarayev (2007). *Introduction to the design of fixed wing micro air vehicles including three case studies*. American Institute of Aeronautics and Astronautics, Inc., Reston, Virginia, USA.

Mula, S. M., and C. E. Tinney (2014). Classical and snapshot forms of the POD technique applied to a helical vortex filament. *In Proceeding of the 32nd AIAA Applied Aerodynamics Conference*, 3257.

Nikfarjam, F. and A. Sohankar (2015). Study of hysteresis associated with power-law fluids past square prisms arranged in tandem. *Ocean Engineering* 104, 698-713.

Oberleithner, K., M. Sieber, C. N. Nayeri, C. O. Paschereit, C. Petz, H. C. Hege, B. R. Noack and I. Wygnanski (2011). Three-dimensional coherent structures in a swirling jet undergoing vortex breakdown: stability analysis and empirical mode construction. *Journal of Fluid Mechanics* 679, 383–414.

Ol'shanskii, M. A. and V. M. Staroverovon (2000). On Simulation of outflow boundary conditions in finite difference calculations for incompressible fluid. *International Journal in Numerical Methods in Fluids* 33, 499.

Peng, D. and J. W. Gregory (2017). Asymmetric distributions in pressure/load fluctuation levels during blade-vortex interactions. *Journal of Fluid and Structures* 68, 58–71.

Perrotta, G. and A. R. Jones (2017). Unsteady forcing on a flat-plate wing in large transverse gusts. *Experiments in Fluids* 58(8), 101-112.

Prakash, C. and S. V. Patanker (1985). A Control Volume Based Finite Element Method for solving the Navier-Stokes Equations Using Equal Order Velocity Pressure Interpolation. *Numer Heat Transfer* 8, 259.

Roshko, A. (1954). On the development of turbulent wakes from vortex streets, National Advisory Committee for Aeronautics, NACA Technical Report 1191.

Saabas, H. J. and B. H. Baliga (1994). Co-located equal-order control volume finite Element method for multidimensional incompressible fluid flow part I: Formulation. *Numerical Heat Transfer Part B*, 26-409.

Samani, M. (2014). *Study of Coherent Structures in Turbulent Flows Using Proper Orthogonal Decomposition*. Ph. D. thesis, University of Saskatchewan, Canada.

Schneider, G. E. and M. J. Raw (1987). A Skewed Positive Influence Coefficient Upwinding Procedure for Control Volume Based Finite Element Convection Diffusion Computation. *Numerical Heat Transfer* 11, 363.

Sirovich, L. (1987). Turbulence and the dynamics of coherent structures part I: coherent structures. *Quarterly of Applied Mathematics* 45(3), 561-571.

Streitlien, K., G. S. Triantafyllou and M. S. Triantafyllou (1996). Efficient foil propulsion through vortex control. *American Institute of Aeronautics and Astronautics Journal* 34(11), 2315-2319.

Tang, G. Q., C. Q. Chen, M. Zhao and L. Lu (2015). Numerical simulation of flow past twin near-wall circular cylinders in tandem arrangement at low Reynolds number. *Water Science and Engineering* 8(4), 315-325.

Unal, M. and D. Rockwell (1988). On vortex formation from a cylinder, Part 2, Control by splitter-plate interference. *Journal of Fluid Mechanics* 190, 513–529.

Vakil, A. and S. I. Green (2013). Numerical study of two-dimensional circular cylinders in tandem at moderate Reynolds numbers. *Transactions ASME Ser I: Journal of Fluids Engineering* 135(7), 071204.

Wang. F. and K. M. Lam (2019). Symmetric and antisymmetric characterization of turbulent flow past a square cylinder of low aspect ratio. *In Proceeding of the Fourth Thermal and Fluids Engineering Conference*, Las Vegas, NV, USA, 767-775.

Weiland, C. and P. Vlachos (2007). Analysis of the parallel blade vortex interaction with leading edge blowing flow control using the proper orthogonal decomposition. *In proceedings of ASME Fluids Engineering Division Summer Meeting collocated with the fifth Joint ASME/JSME Fluid Engineering Conference*, San Diego, California, USA, 1523-1533.

Zdravkovich, M. (1987). Review of flow interference between two circular cylinders in various arrangements. *Transactions ASME Ser I: Journal of Fluids Engineering* 99, 618.

Zehner, P., F. Falissard and X. Gloerfelt (2018). Aeroacoustic study of the interaction of a rotating blade with a Batchelor vortex. *American Institute of Aeronautics and Astronautics Journal* 56, 629–647.

Zhang, Z., Z. Wang and I. Gursul (2020). Lift Enhancement of a Stationary Wing in a Wake. *American Institute of Aeronautics and Astronautics Journal* 58(11), 4613-4619.